Exploring Rochelle Salt Aqueous Solutions for Supercapacitors: Transport, Stability, and Performance

Hamza Kahri, Chalal Tachouaft, Yanzhuo Li, Ziwei Chen, Mérièm Anouti, and Georgios Nikiforidis*

This study examines the thermal, transport, and electrochemical properties of Rochelle salt (SPTa, $KNaC_4H_4O_6 \cdot 4H_2O$) aqueous solutions for energy storage applications. SPTa exhibits eutectic melting ($-38\,°C$), crystallization, density variations (e.g., $0.25\ g\ cm^{-3}$ at $25\,°C$ for $2.0\ mol\ dm^{-3}$), and high ionic conductivity ($70\ mS\ cm^{-1}$ at $25\,°C$ for $1.0\ mol\ dm^{-3}$), which increases with temperature and concentration. Ionic transport follows the Arrhenius and Vogel–Fulcher–Tammann models, indicating low activation energies for ion mobility, especially below $8\,°C$. The Walden plot analysis suggests that most ions remain dissociated in the solution, while the thermodynamic parameters from the activated state of viscosity indicate strong chelation and molecular structuring effects. Cyclic voltammetry of symmetric supercapacitors with activated carbon electrodes in $1.0\ mol\ dm^{-3}$ SPTa confirms double-layer capacitive behavior with a $2.5\,V$ electrochemical window. Galvanostatic charge/discharge tests reveal an energy density of $35\ Wh\ kg^{-1}$, excellent cycling stability ($10\,000$ cycles), and high coulombic efficiency ($>97\%$). Electrolyte evaporation and electrode degradation require further optimization for long-term stability. These findings highlight SPTa as a cost-effective and sustainable candidate for electrochemical energy storage.

1. Introduction

Supercapacitors (SCs) have emerged as a critical energy storage technology, offering a unique combination of high-power density (in the order of $102\ W\ kg^{-1}$), long cycle life ($>20\,000$ cycles), and rapid charge/discharge capabilities. Unlike batteries, traditional SCs store energy electrostatically, thereby avoiding chemical reactions and enabling hundreds of thousands of cycles with minimal performance degradation. Depending on the charge storage mechanism and active materials, SCs are classified into electrochemical double-layer capacitors (EDLCs), pseudocapacitors, and hybrid capacitors. SCs can balance energy and power density, making them particularly suitable for scenarios that require fast energy delivery and high load currents. Their inherent flexibility in size, design, and operating temperature ($-40–25\,°C$) makes them ideal for numerous applications, including modern electronics, rail systems, regenerative power, and smart energy harvesting systems.[1]

H. Kahri, C. Tachouaft, M. Anouti
Laboratoire PCM2E
Université de Tours
Parc de Grandmont, 37200 Tours, France

Y. Li, Z. Chen, G. Nikiforidis
Institute for Materials Discovery
Marshgate, University College London
London E20 2AE, UK
E-mail: Georgios.nikiforidis@ucl.ac.uk

Their performance depends on factors such as the specific capacitance of the active materials and operating voltage, which directly influence their energy and power density. Innovations in structured and porous electrode materials such as graphene, metal oxides/hydroxides/chalcogenides, and conducting polymers have driven recent advancements in this field,[2,3] along with the precise electrolyte engineering of robust electrolytes.[4,5] Electrolytes play a crucial role as ionic conductors, directly impacting the operating voltage and specific capacitance of SCs.

Efforts to extend the electrochemical window of SC systems while at the same time asserting their electrochemical stability have led to the exploration of various electrolytes, including organic solutions, ionic liquids, deep eutectic solvents, and solid/quasi-solid electrolytes in both concentrated and diluted conditions.[6–9] Organic electrolytes and ionic liquids provide a broader window ($>2.8\,V$), improving energy density, but face drawbacks like flammability, toxicity, high cost, low conductivity and viscosity at times, and moisture sensitivity.[10] Solid/quasi-solid electrolytes, such as hydrogels and aerogels, offer good mechanical properties and thermal performance but are limited by lower ionic conductivity.[5]

Aqueous electrolytes remain appealing due to their low cost, eco-friendliness, ease of processing, and high ionic conductivity. However, the water-splitting reaction at $\approx 1.23\,V$ remains a hurdle. Recent advances, such as "water-in-salt" electrolytes[9,11] with sodium perchlorate ($NaClO_4$), lithium nitrate ($LiNO_3$), and lithium bis(trifluoromethanesulfonyl) imide (LiTFSI) salts, have achieved wide stability windows ($\approx 3\,V$) as well as improved ion transport and safety. However, the high salt content required in these systems may limit their cost-effectiveness for large-scale applications. Besides, other concentrated aqueous solutions (e.g., manganese nitrate) have shown promise due to their intriguing characteristics, i.e., eutectic-like behavior where water

is almost completely distributed over the solvation shell of ions.[12] The decrease in water concentration in saturated electrolytes somewhat increases the potential window, as is the case with potassium/sodium/manganese acetate (Kac, NaAc, (Mn(Ac)$_2$) and potassium formate (KOOCH) solutions.[9,13,14]

In the search for other emerging water-soluble organic conducting salts, potassium sodium tartrate tetrahydrate (SPTa, Rochelle salt) is investigated in this study. Rochelle salt is a naturally occurring, water-soluble compound widely recognized for its piezoelectric (SPTa exhibits two Curie points at $-18°$ and $24°$ C, respectively),[15] ferroelectric, and paraelectric phase properties from low to high temperatures,[16] which makes this crystal useful in technological applications such as sensors, actuators, and SCs.[17–19] For the latter, a study based on an asymmetric piezo-SC using a nickel/Rochelle salt nanowire array as a cathode and a polypyrrole/ nickel/Rochelle nanowire array as an anode reported an energy density of 166 Wh kg^{-1}. Other instances where Rochelle salt has been utilized include electrodeposition (Cu-Zr thin film[20]), as crystals for antimicrobial activity,[21] and as an inhibitor for the alkaline solution(s) of aluminum-air batteries.[22]

Rochelle salt is water-soluble, enabling its use in aqueous-based electrolyte systems that are safe, nonflammable, and environmentally friendly. The tartrate molecule is found to lie approximately in three planes, the planes of each half of the molecule being inclined at 60° to the plane of the carbon atoms.[15] These molecules are bonded to sodium and potassium atoms both directly and through the medium of water molecules. Herein, a systematic investigation was conducted on aqueous Rochelle salt electrolytes (0.5–2.0 mol dm^{-3} KNaC$_4$H$_4$O$_6$·4H$_2$O) alongside a lithium analog (0.5 mol dm^{-3} C$_4$H$_4$Li$_2$O). The properties of tartrate, sodium, and potassium ions in an aqueous environment were examined with regard to their volumetric, thermal, and transport characteristics. These electrolytes were then incorporated into symmetric two-electrode EDLCs using activated carbon (AC) electrodes. The dual cation nature (K$^+$ and Na$^+$) contributes to a synergistic ion transport mechanism, while the complexation behavior of the tartrate anion influences solvation dynamics and water activity factors critical for expanding the voltage window. The SCs demonstrated a broad electrochemical window (2.5 V), notable specific capacitance (>80 F g^{-1}), high energy density (35 Wh kg^{-1}), and excellent stability (10 000 cycles at 2.5 A g^{-1}), establishing the viability of such aqueous electrolytes for practical energy storage and conversion applications.

2. Results and Discussion

2.1. Thermal and Volumetric Properties of Rochelle Salt Aqueous Solutions

The Fourier transform infrared spectroscopy (FT-IR) spectra of potassium sodium tartrate tetrahydrate (SPTa) salt and its aqueous solutions (**Figure 1**a) confirm the presence of carboxylate functional groups, indicating the conversion of carboxylic acid into a carboxylate salt. Characteristic stretching vibrations corresponding to O—H (≈3400 cm^{-1}), C—H (≈2900 cm^{-1}), C=O (≈1600 cm^{-1}), C—O

(≈1400 cm^{-1}), and carboxylate anion (≈1300 cm^{-1}) are observed, consistent with previously reported data.[16,23]

The thermal properties of these solutions (Figure 1b) exhibit a eutectic melting behavior upon heating from -60 to $100°$C, followed by a liquidus transition, with the onset of melting varying depending on the solution composition. During cooling, all samples display distinct crystallization peaks between -25 and $-45°$C, suggesting supercooling effects. The eutectic composition ($x_E = 0.38$) and temperature ($T_E = -38°$C) were determined from the liquidus data and plotted in the phase diagram (Figure 1c). The melting points range from $-16°$C (for 1.5 mol dm^{-3} SPTa) to $0°$C (2.0 mol dm^{-3} SPTa), while the pure salt exhibits a melting point of 68 °C, in agreement with previous studies.[23] No phase transitions are observed above 3 °C, regardless of composition. The density variations (ρ) of the aqueous SPTa solutions were measured between 10 °C and 60 °C at different salt concentrations, with their logarithmic variations against temperature presented in Figure 1d. As expected, ln(ρ) decreases linearly with increasing temperature and rises with higher SPTa concentrations. Notably, Figure 1d illustrates a 20% increase in density for a fourfold increase in salt concentration (0.5 $\rightarrow$ 2 mol dm^{-3}) in the same range with other aqueous solutions containing KOH, Mn(NO$_3$)$_2$·6H$_2$O, Mn(Ac)$_2$, and Na$_2$SO$_4$ salts.[12,13,24]

Figure 2a,b presents the ionic conductivity of four aqueous sodium tartrate tetrahydrate (SPTa) solutions in different concentrations (i.e., 0.5 $\rightarrow$ 2.0 mol dm^{-3}) within -20–60 °C. The solubility limit lies over 2.0 mol dm^{-3}, as illustrated in Figure S2, Supporting Information. The ionic conductivity (σ) increases with temperature (i.e., higher ionic mobility) and concentration (i.e., higher ion availability) and reaches a maximum value of 140 mS cm^{-1} at 60 °C for a representative concentration of 2.0 mol dm^{-3} SPTa. At room temperature, the σ value reaches 70 mS cm^{-1}, which aligns with other aqueous solutions, such as KOH, NaOH, and H$_2$SO$_4$.[25] Besides, the lithium analog, dilithium tartrate (Li$_2$Ta, Figure 2c), yields similar ionic conductivity values ranging between 20 and 60 mS cm^{-1}, reinforcing the potential for such salt to be used for electrochemical applications.

Figure 2d presents molar conductivity (λ) as a function of the square root of concentration, showing a linear trend, viz., this aqueous electrolyte is a "strong" electrolyte as it dissociates entirely in solution across temperatures from 10 to 60 °C. By extrapolating λ, the limiting molar conductivity ($\lambda_o \rightarrow$ 110–255 S mol^{-1} cm) is extracted, which is essential for studying ion-solvent interactions and calculating dissociation constants or transport numbers for strong electrolytes. Figure 2e indicates that the aqueous solutions with 0.5 and 1.0 mol dm^{-3} SPTa follow the Arrhenius model,[26] which relates temperature to the energy needed for ion movement. There is, however, a distinct transition at 8 °C where the activation energy (E_a) significantly decreases at higher temperatures, reaching -13 kJ mol^{-1} for both concentrations (**Table 1**), indicating a more efficient conduction mechanism, i.e., proton hopping (Grotthus mechanism[27]) reported in several other electrolytes.[28] At temperatures lower than 8 °C, E_a reaches -102 kJ mol^{-1} and -88 kJ mol^{-1} for 0.5 and 1.0 mol dm^{-3} SPTa, respectively. At higher SPTa concentrations (1.5 and 2.0 mol dm^{-3}), the Vogel–Fulcher–Tammann (VFT) model[26] was implemented (Figure 2f). The latter incorporates three fitting parameters, namely, σ_0, E^σ_{psa}, and T_0.

Batteries & Supercaps

Research Article
doi.org/10.1002/batt.202500259

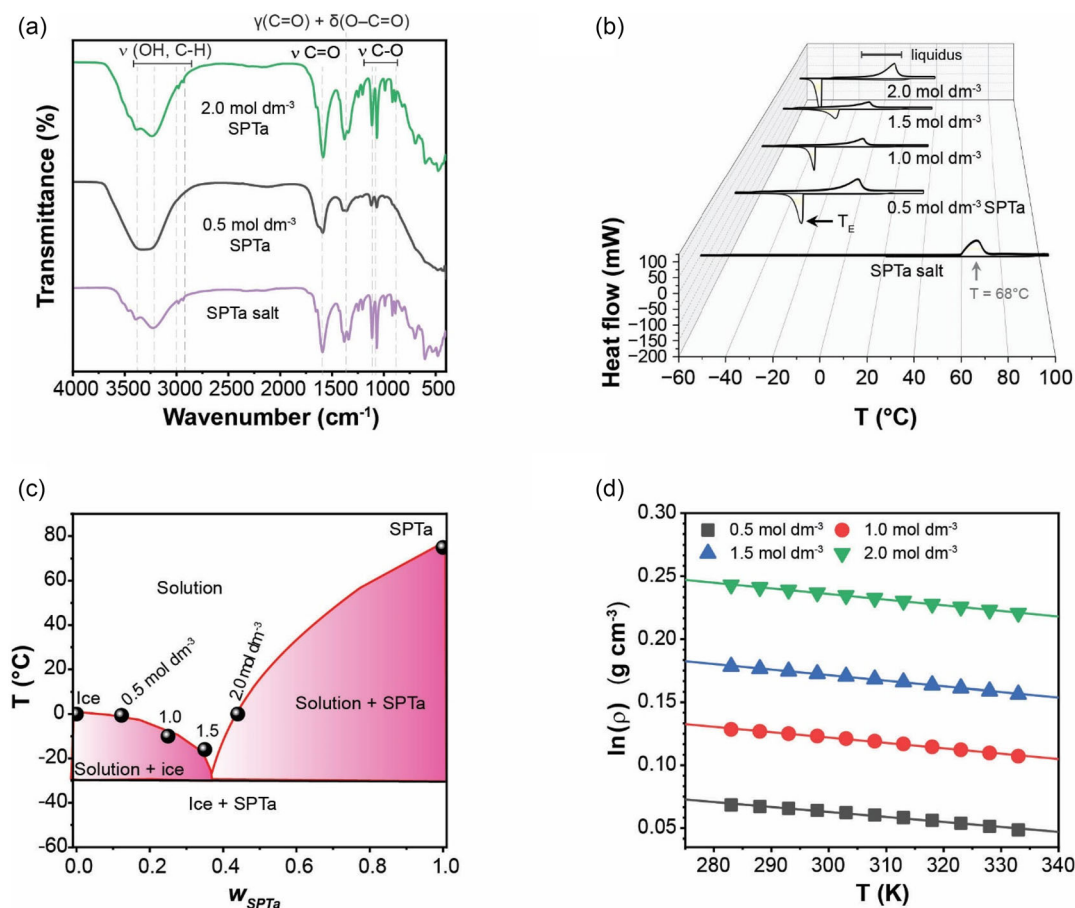**Chemistry
Europe**

European Chemical
Societies Publishing

Figure 1. a) FT-IR spectrum of potassium sodium tartrate tetrahydrate salt (SPTa) and two aqueous solutions (0.5 and 2.0 mol dm^{-3} SPTa). b) Thermograms of the SPTa solutions. c) Eutectic diagram of the aqueous SPTa solution incorporating the position of the four electrolytes used in this study. d) Evolution of density with temperature for the same electrolytes.

The slope of $\ln(\sigma) = f\left(\frac{1}{T-T_0}\right)$ yields a pseudoactivation energy "E_{psa}^{σ}" describing the ionic mobility. T_0 termed ideal glass transition temperature is a corrective term used in the VTF model to describe the deviation from the Arrhenius model,[29] i.e., the $\frac{T_g}{T}$ is close to 1 where T_g describes the glass transition temperature. The E_{psa}^{σ} values from the VTF model are lower than the ones extracted from the Arrhenius fitting between −2.75 and −2.95 kJ mol^{-1} while the T_0 values varied linger at 175 K (−98 °C), in line with other aqueous systems.[12] Overall, the activation energy values suggest that all SPTa solutions offer a low-energy barrier for ion transport, making them promising candidates for electrochemical applications.

2.2. Viscosity and Ion Solvation of Rochelle Salt Aqueous Solutions

A balance between high conductivity and low viscosity is essential for electrolytes in energy storage applications to ensure efficient ion transport and high energy storage capacity. **Figure 3**a displays the evolution of the dynamic viscosity within 10 and 60 °C at the four aqueous SPTa concentrations. The viscosity of the solution increases with higher amounts of SPTa and at room temperature reaches a maximum of 3.5 mPa s at 2.0 mol dm^{-3},

low enough to support good ionic mobility (Figure 2a, >40 mS cm^{-1}) and comparable to conventional aqueous electrolytes such as LiCl, ZnSO$_4$, and Mn(Ac)$_2$.[13,30,31] As the temperature increases, the viscosity shifts to values smaller than 2.0 mPa s, leading to linear-fitted plots (Figure 3b). This trend suggests that the thermal energy disrupts ion-solvent and ion-ion interactions, reducing resistance to flow.

According to Eyring's theory,[13] the liquid structure can be considered a quasi-crystal network where the molecules move in the liquid state in parallel layers by sliding planes. A molecule must acquire enough energy to overcome an activation barrier and jump into an available "hole". This energy barrier represents the activated state, influenced by molecular organization and intermolecular interactions. The Gibbs energy variation in this process can be expressed in terms of enthalpy (interactions) and entropy (disorder) of the transient state (Figure 3c). The activation viscous flux energy values ($\Delta H^{\#}$) linger between 15 and 17 kJ mol^{-1} and increase linearly with salt concentration, owing to the stronger ion–solvent and ion–ion interactions that may require additional energy to overcome. The evolution of activation entropy ($\Delta S^{\#}$) is constant (41 J mol^{-1} K^{-1}, Figure 3c) throughout the concentration range, suggesting that the system retains some degree of molecular flexibility, which improves ionic
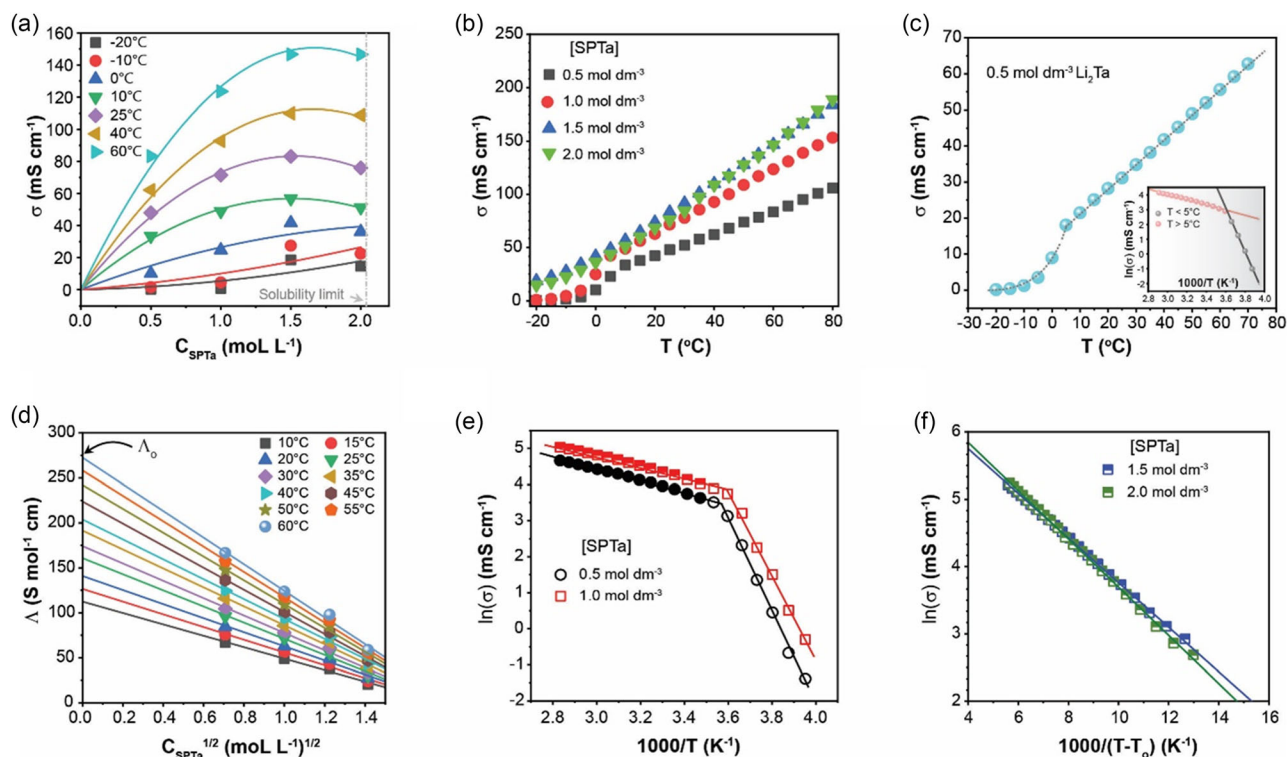
Figure 2. Ionic conductivity (α) as a function of sodium tartrate tetrahydrate (SPTa): a) concentration in aqueous media at different temperatures (−20–60 °C). b) Ionic conductivity of different concentrated SPTa solutions as a function of temperature. c) Ionic conductivity of dilithium tartrate (0.5 mol dm^{-3} Li$_2$Ta). Inset shows the Arrhenius plots of the ionic conductivity. d) Molar conductivity (Λ) versus the square root of concentration ($C_{SPTa}^{1/2}$) between temperatures ranging from 10 to 60 °C. e) Modeling of ionic conductivity by the Arrhenius equation for aqueous solutions containing 0.5 and 1.0 mol dm^{-3}. Inset shows the plots for 1.5 and 2.0 mol dm^{-3} SPTa. f) Modeling of ionic conductivity by the VFT correlation for aqueous solutions containing 1.5 and 2.0 mol dm^{-3} SPTa.

Table 1. Arrhenius and VTF fitting parameters for the aqueous SPTa electrolytes investigated in this study. The data are extracted from Figure 2d,e.

Arrhenius	C_{SPTa} [mol dm^{-3}]	$\ln(\sigma_0)$ [mS cm^{-1}]	E_a^σ [kJ mol^{-1}]	R^2
	0.5 (T < 8 °C)	9.2	−102	0.995
	0.5 (T > 8 °C)	50.0	−13	0.997
	1.0 (T < 8 °C)	9.5	−88	0.994
	1.0 (T > 8 °C)	45.9	−13	0.997
VTF	C_{SPTa} (mol dm^{-3})	T_0 (K)	E_{psa}^σ (kJ mol^{-1})	R^2
	1.5	174	−2.75	0.999
	2.0	176	−2.97	0.999

transport. The value of the $\Delta S^{\#}$ is constant, close to the one of water (38 J mol^{-1} K^{-1}), and slightly higher than other reported aqueous electrolytes.[32]

Moreover, the Walden plot in Figure 3d provides a good representation of the ionicity transport properties of these solutions (even though it is more suited for ionic liquids). The solid gray line represents the ideal Walden behavior assigned to a diluted KCl solution,[33] and the direction of deviation and its magnitude from this line describe the degree of ionization. Deviation from the ideal line signifies a gradual reduction in the ionic nature of the solution because of ion aggregation. The Walden slope (α) values lie between 0.86 and 0.92 (i.e., a small deviation from the

ideal line), suggesting that most of the salt is dissociated and the ions are more independently mobile.

The differences in the molecular organization of the SPTa electrolytes were examined by applying the Jones–Dole–Kaminsky (JDK) relationship[34] for moderately concentrated solutions,[26] i.e., >0.05 mol dm^{-3}. **Figure 4**a shows the influence of temperature on ion-ion and ion-solvent interactions. The extracted B values are positive (**Table 2**), indicating that the salt induces a structuring effect on the solvent, enhancing the organization and stability of the solution. These values are linked to the hydrodynamic radius r_h^B, through Einstein's theory of viscosity based on the model of solid spheres in solution and the solvent crown around solvated ions.[26] The relation between B and r_h^B allows for the estimation of the sphere's dimension around the solvated ion, as shown in Figure 4b. The solvation radius follows a similar trend to the aqueous manganese nitrate,[12] where only anion–cation interactions are present. However, the values are twofold higher (ranging between 0.41 and 0.46, Table 2), close to alkali cations such as Li, Na, and K,[35] suggesting stronger solvation and molecular structuring effects due to molecular aggregation. In contrast, aqueous manganese acetate solutions[13] show a different behavior. Unlike nitrate, acetate facilitates both solvation and ligand-type complexation. In this case, carboxylate (COO$^-$) groups chelate Mn^{2+}, forming hydrogen bonds that are sensitive to temperature variations.
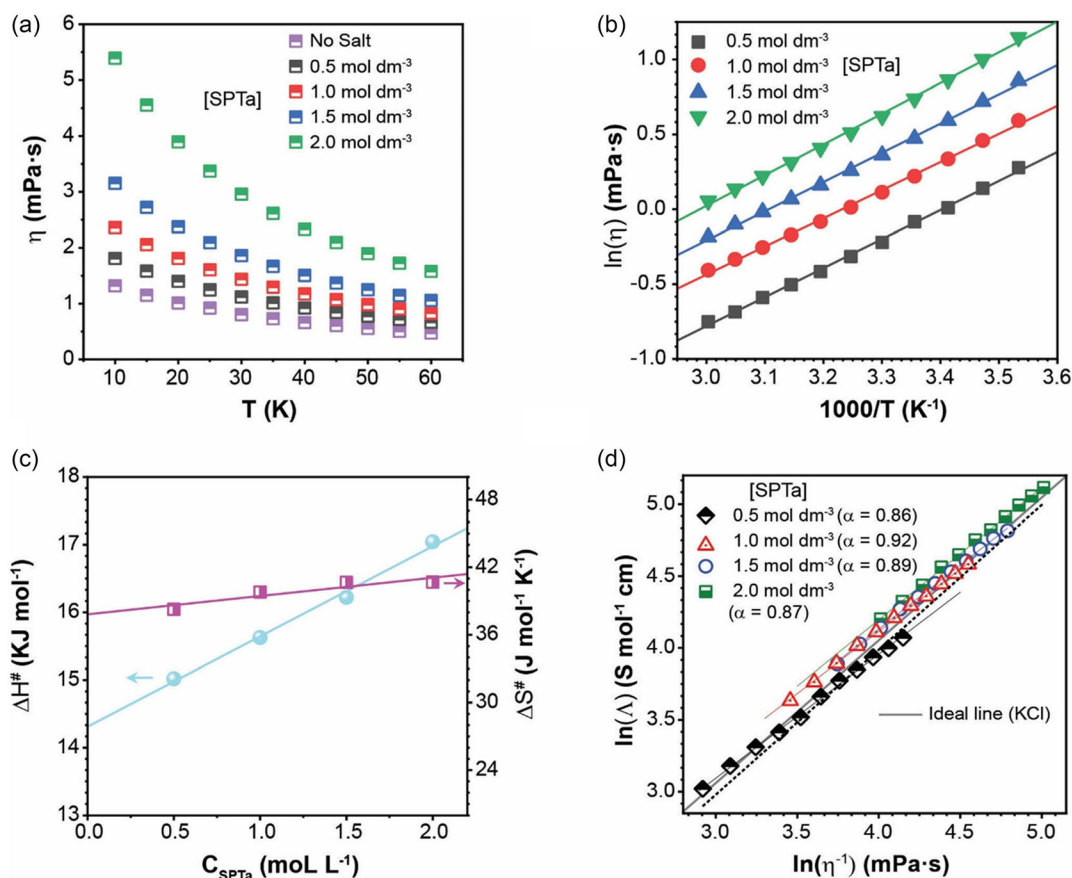
Figure 3. a) Variation of viscosity (η) with temperature (T) for solutions of different SPTa salt concentrations (0.5 to 2.0 mol dm^{-3}) and a salt-free sample. b) Evolution of the natural logarithm of viscosity (ln(η)) as a function of inverse temperature for the same concentrations. c) Thermodynamic parameters of viscosity activation, enthalpy ($\Delta H^{\#}$), and entropy ($\Delta S^{\#}$) plotted against salt concentration (C_{SPTa}). d) Walden plot illustrating the relationship between molar conductivity (Λ) and the reciprocal of viscosity (η^{-1}).
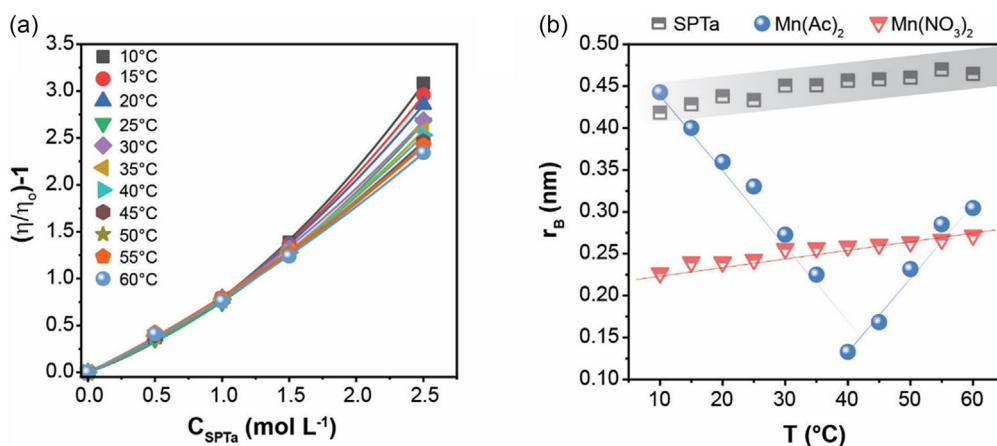

Figure 4. a) Dynamic viscosity of the SPTa aqueous electrolytes at different concentrations. b) Effective hydrodynamic radius of the SPTa system. For comparison, data from the aqueous Mn(NO$_3$)$_2$-H$_2$O[12] and Mn(Ac)$_2$[13] systems are also included.

2.3. Electrochemical Energy Storage with the Rochelle Salt Aqueous Solutions

Figure 5a shows cyclic voltammograms (CVs) of two-electrode SCs in the presence of all four solutions, revealing mostly rectangular-shaped CV curves. This behavior, which is also observed in the three-electrode CVs (Figure S3, Supporting Information), is characteristic of the EDLC of porous AC structure with a broad particle size distribution[29] (Figure 5b), validating the feasibility of these electrolytes for energy storage applications. The surface tension of the SPTa solution is typical of aqueous solutions,[36] reaching 73 mN m^{-1} $\pm$ 0.81 (Figure 5b for 1.0 mol dm^{-3} SPTa)

Batteries & Supercaps

Research Article
doi.org/10.1002/batt.202500259

Chemistry Europe
European Chemical
Societies Publishing

Table 2. Values of B coefficients from the JDK relationship together with solvation radius r_h^B for the SPTa electrolytes at different temperatures.

T [°C]	10	20	30	40	50	60
B [L mol^{-1}]	0.477	0.548	0.596	0.627	0.635	0.653
r_h^B [nm]	0.418	0.438	0.451	0.457	0.460	0.465

at room temperature, suggesting adequate wettability of the AC electrode. The electrochemical window of the symmetric SCs can be extended up to 2.5 V at the expense of a lower fill factor, viz., 67% for 1.0 mol dm^{-3} SPTa compared to 76% for an electrochemical window of 2.0 V, suggesting that the capacitive behavior is hindered by oxidation reaction(s) at higher cell voltage (e.g., water splitting). There are no stark differences in the CV behavior (rectangular shape, oxidation potential) and normalized current

density upon a fourfold increase in the SPTa concentration (0.5 → 2 mol dm^{-3}), likely due to the saturation of double-layer formation and limited improvement in ion transport kinetics at higher ionic strength.[37] It should be noted that the equally conductive lithium analog (Li$_2$Ta, Figure 2c) exhibits a similar rectangular CV shape (Figure S4, Supporting Information), confirming that both SPTa and its lithium analog (Li$_2$Ta) provide comparable ionic conductivity and electrochemical stability within the investigated electrochemical window.

Following the CVs, galvanostatic charge-discharge (GCD) curves at different normalized currents (0.25–2.5 A g^{-1}) are shown in Figure 5c in the presence of 1.0 mol dm^{-3} SPTa. A low salt concentration is more cost-effective, considering that there is no significant improvement in electrochemical performance at higher amounts (CV curves of Figure 5a) and the physicochemical properties are
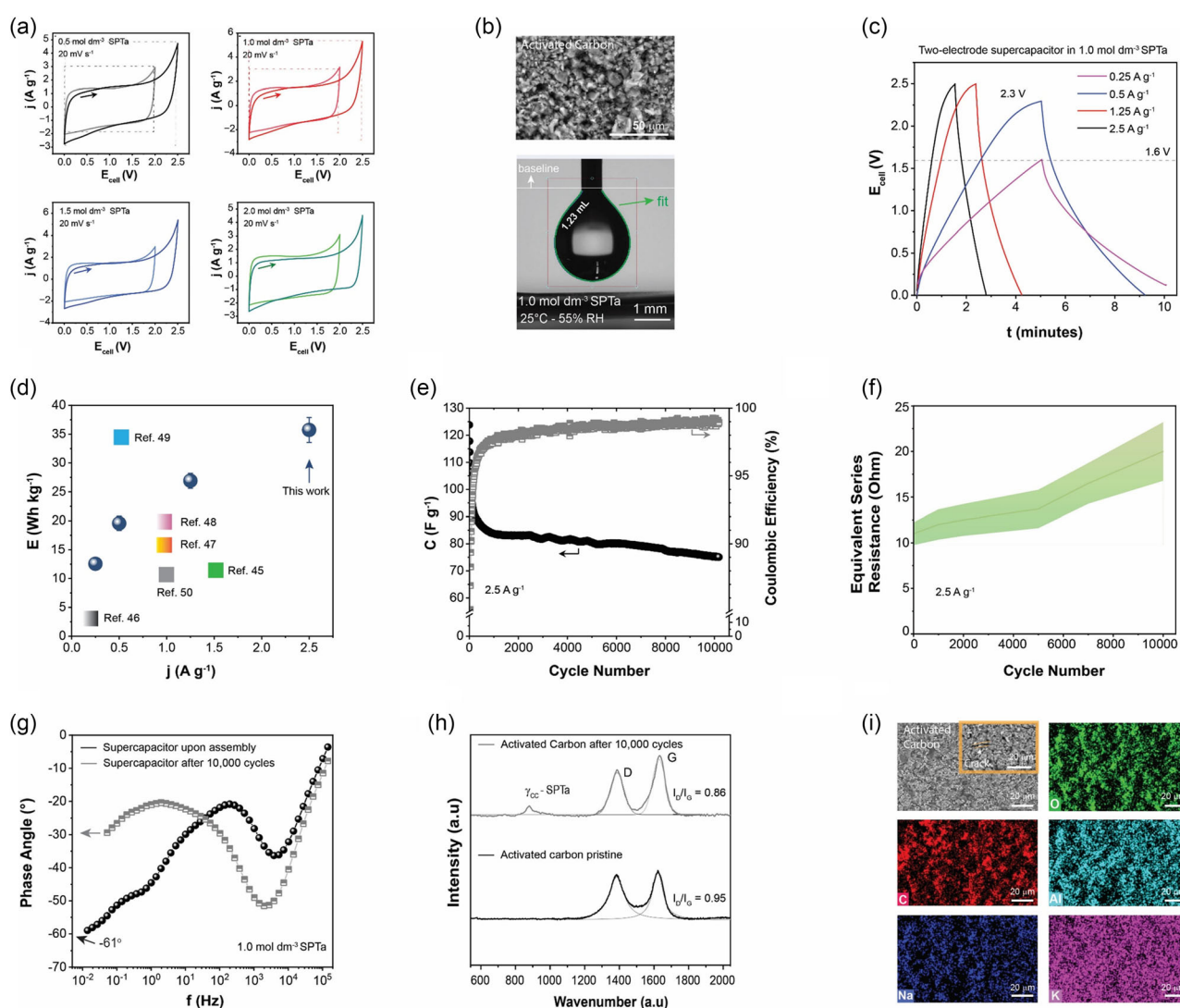

Figure 5. a) CVs of the two-electrode SC with various aqueous SPTa solutions at a scan rate of 20 mV s^{-1}. The measurements were conducted at room temperature. b) SEM image of the pristine AC. The bottom picture depicts the surface tension of the 1.0 mol dm^{-3} SPTa solution. c) GCD curves for an SC under a 1.0 mol dm^{-3} SPTa solution at various current densities. d) Energy density of the SC under the same solution, compared with other studies. The average of three measurements is shown here. e) Cycling stability of the SC over 10 000 cycles, demonstrating specific capacitance and coulombic efficiency. f) ESR during the cycling protocol. The shaded region represents the experimental error or measurement variability (95% confidence interval). g) Bode plots of phase angle versus frequency before and after GCD cycling. h) Raman spectroscopy of the AC electrode before and after GCD cycling. i) Top-view SEM along with EDS mapping of the cycled AC electrode.

quite similar (e.g., Figure 2b and 3d). The current price for Rochelle salt is \$60.30 per 100 g^{-1} giving an approximate electrolyte cost of \$0.85 (i.e., 1 mol dm^{-3} × 282.22 g mol^{-1} × 0.005 L × 0.603\$ g^{-1}) for 5 mL of solution, higher than the one for the aqueous sodium sulfate and potassium hydroxide solutions (Na$_2$SO$_4$ → \$0.21, KOH → \$0.095) but lower than nonaqueous electrolytes (e.g., acetonitrile with lithium bis(trifluoromethanesulfonyl)imide salt, \$13.9).

The triangular shapes demonstrate double-layer capacitive behavior.[38] Under these current rates, the maximum energy density achieved is ≈35 Wh kg^{-1} (for 10 mA, that is 2.5 A g^{-1}, Figure 5d), superior to other symmetric SCs using aqueous solutions and AC electrodes (e.g., KOH, Na$_2$SO$_4$, NaNO$_3$, LiTFSI, H$_2$SO$_4$, K$_2$SO$_4$, and Li$_2$SO$_4$).[39–45] The long-term cycling of the symmetric SC is shown in Figure 5e. The initial specific capacitance of 120 F g^{-1} aligns with similar cells[40,41,44] employing AC under aqueous solutions. After 10–20 cycles, due to electrolyte wetting and ion penetration, it stabilizes around 80 F g^{-1} at 2.5 A g^{-1}, maintaining this level for 10 000 cycles (91.5% specific capacitance retention), while the Coulombic efficiency lingers above 97%. The equivalent series resistance (ESR) that represents the internal resistance of the device[46] is calculated by the inversion of polarity during the GCD cycles. It progressively increases from 11.3 to 19.5 ohm (Figure 5f). The Bode plot (Figure 5g) that typically illustrates how well the SC maintains charge storage across the different frequencies shows a decline in capacitive behavior (−30 vs −62°) owing to electrolyte evaporation, which reduces ion availability and material degradation. The latter is noticeable on the cycled AC surface where the graphitization ratio[38] ($\frac{I_D}{I_G}$) decreased from 0.95 to 0.86 (Figure 5h). This drop may result from surface oxidation or electrolyte decomposition (i.e., oxygen functionalization), leading to increased cell resistance. The loss of graphitic order introduces structural defects, which contribute to the formation of cracks and irregularly shaped particles. These degraded carbon structures are intertwined with SPTa electrolyte components (Na, K) and the current collector (Al), as shown in Figure 5i. Additionally, the emergence of a Raman peak at 846 cm^{-1} associated with the γCC mode of the tartrate ion suggests sustained interaction or accumulation of tartrate species within the porous carbon matrix. This likely reflects structural confinement or adsorption effects, rather than chemical decomposition of the electrolyte.

3. Conclusion

The study of Rochelle salt aqueous solutions as green and cost-effective electrolytes for SCs has demonstrated their promising potential for energy storage. The thermal and volumetric properties of SPTa solutions reveal favorable behaviors such as eutectic melting, crystallization, and density changes with varying concentrations (e.g., 0.25 g cm^{-3} at room temperature for 2.0 mol dm^{-3} SPTa), confirming their suitability for electrochemical applications. The ionic conductivity of SPTa solutions is high (80 mS cm^{-1} at 25 °C for 1 mol dm^{-3} SPTa) and temperature and concentration-dependent. The linear and curvilinear Arrhenius (for 0.5 and 1.0 mol dm^{-3} SPTa) and VFT (for 1.5 and 2.0 mol dm^{-3} SPTa) plots

described the ionic transport behavior, indicating low activation energies (e.g., −102 and −88 kJ mol^{-1} for 0.5 and 1.0 mol dm^{-3} SPTa before 8 °C and −13 kJ mol^{-1} after 8 °C) for ion mobility, which enhances their potential as efficient electrolytes for SCs. The viscosity ranging from 1 to 2.5 mPa·s at room temperature ensures good ionic mobility and minimal resistance to flow. The viscous flux energy (15–17 kJ mol^{-1}) increases with salt concentration, while constant entropy (41 J mol^{-1} K^{-1}) suggests retained molecular flexibility for improved ion transport. Walden plot analysis indicates that most of the dissolved salt remains dissociated, suggesting enhanced ionic mobility and good ionicity very close to the ideal line. Additionally, the thermodynamic parameters from the activated state of viscosity according to the Erring theory and the JDK model for solvation indicate that ion-solvent and ion–ion interactions play a crucial role in ion-transport properties.

The electrochemical energy storage performance of the SCs with SPTa as the electrolyte and AC as electrodes is promising, with rectangular CVs indicative of electric double-layer capacitance behavior. The SCs under 1.0 mol dm^{-3} SPTa reach an energy density of 35 Wh kg^{-1} at a normalized current density of 2.5 A g^{-1}. The long-term cycling stability is manifested by 10 000 cycles (stabilizing at 80 F g^{-1}) while the high coulombic efficiency (>97%) further emphasizes the viability of SPTa solutions for practical energy storage applications. However, the study also identifies challenges, such as electrolyte evaporation and electrode degradation, as evidenced by changes in the graphitization ratio and surface morphology of the AC electrodes after cycling.

Overall, SPTa solutions exhibit excellent ionic conductivity, electrochemical stability, and energy storage performance, making them strong candidates for use in SCs. Further optimization of electrode materials is required to improve their long-term stability and address the challenges of material degradation during cycling.

4. Experimental Section

Electrolyte Formulation

Potassium sodium tartrate tetrahydrate (SPTa, KNaC$_4$H$_4$O$_6$·4H$_2$O, 99.5%) and dilithium tartarate (Li$_2$Ta, 99.8%) were purchased from Sigma-Aldrich and used as received. A known quantity of crystalline potassium sodium tartrate tetrahydrate (Figure S1, Supporting Information) is added to 5 g of deionized water and stirred to create a homogeneous mixture according to the following reaction

$$KNaC_4H_4O_6 \cdot 4H_2O \rightarrow K^+ + Na^+ + C_4H_4O_6^{2-} + 4H_2O \tag{1}$$
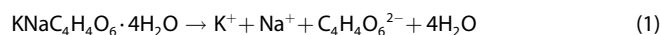
All four prepared solutions with concentrations of 0.5, 1.0, 1.5, and 2.0 mol dm^{-3} remain liquid at 25 °C. The solubility limit of this salt in water was ≈2.5 mol dm^{-3} (Figure S2, Supporting Information). The lithium tartarate solution used as a comparison was prepared in a similar manner.

Physicochemical Characterization of Electrolytes

The ionic conductivity measurements were performed with a multi-channel conductivity meter (Biologic, France) based on a frequency response analyzer (MCM 10) connected to a Peltier-based temperature

Batteries & Supercaps

Research Article
doi.org/10.1002/batt.202500259

Chemistry Europe
European Chemical
Societies Publishing

control unit with ten slots (WTSH 10, Biologic). The measurements were recorded between −20 and 60 °C in sealed cells with Pt parallel-plate electrodes, protecting the samples from air exposure. The viscosity measurements were carried out between 10 and 60 °C ($\pm$0.02 °C) using an Anton Paar digital rolling-ball viscometer (Lovis 2000M/ME). The uncertainty of the measurements was $\approx 4 \times 10^{-5}$ g cm^{-3} for the density and 2% for the ionic conductivity. Differential scanning calorimetry (DSC) was performed with a PerkinElmer DSC 4000 calorimeter. The samples were initially cooled to −23 °C, followed by a five-minute isothermal plateau at this temperature, then heated up to 81 °C at a rate of 5 °C min^{-1}. The FT-IR spectra of potassium sodium tartrate tetrahydrate salt and the aqueous solutions were recorded with a Shimadzu IRAffinity-1S. The spectra resolution was 4 cm^{-1}, and data were collected in the transmittance between 4000 and 400 cm^{-1}. XRD spectra of the salt were collected using a D8 Advance diffractometer (Bruker) with Ni-filtered Cu Kα radiation (1.54 Å, generator settings: 40 kV, 40 mA) and a Lynx-eye detector. The solution's surface tension (pendant drop) was measured using an Ossila contact angle goniometer (Ø$_{needle}$ = 0.47 mm, video recording at 30 frames per second). The cost calculation for the aqueous electrolytes was based on prices obtained from the Sigma-Aldrich website (www.sigmaaldrich.com).

Material Characterization and Supercapacitor Fabrication

The electrodes are supplied by Blue Solutions (France) and consist of AC, poly(vinylidene difluoride) (PVDF), and carbon black in an 80:10:10 weight ratio, coated onto aluminum foil. The AC loading was $\approx$5 mg cm^{-2} per unit area. Swagelok-type cells (Biologic, France) were used with electrodes of 1 cm diameter (geometrical area: 0.78 cm^2) that served as both anode and cathode. The Brunauer–Emmett–Teller surface area of the electrodes was reported in a previous study[26] (i.e., 2270 m^2 g^{-1}). The separator (Whatman filter paper, GF/C, Ø = 12 mm) was predried at 80 °C for 12 h before cell assembly. An electrolyte volume of 150 µL was added dropwise from a micropipette (Mettler Toledo) between each layer. After assembly, the cells (SCs) underwent a 12-hour wetting to ensure complete electrolyte absorption.

Top-view electron microscopy pictures of the AC electrode were acquired by scanning electron microscopy (SEM; Hitachi TM4000Plus) using a tungsten wire electron source. The distributions of the constituent elements in the electrode layers were investigated through energy-dispersive X-ray (EDS) spectroscopy (Bruker, SCU) with an acceleration voltage of 10–15 kV. Ex-situ Raman spectra of the AC electrodes were obtained by an inViaconfocal Raman microscope (Renishaw) under a 532 nm laser excitation and a 10 or 20× magnification lens. The deconvolution of the D and G bands was done by Lorentzian fitting.

Electrochemical Characterization of the Supercapacitor

The GCD cycling, CV, and potentiostatic impedance spectroscopy (PEIS) measurements of the two-electrode SC were carried out by a Biologic VMP3 potentiostat (Biologic, France). The CVs were performed relative to the set electrochemical window at designated scan rates (1–100 mV s^{-1}) and normalized with respect to the active mass of the carbon (0.05 mg). For the three-electrode CVs, a Pt wire reference electrode (PalmSens) and a Pt foil counter electrode (Alvatek Ltd.) were used. The energy density (E, Wh kg^{-1}), which is the amount of energy stored per unit of mass, was derived from the GCD curves by applying equations reported in previous studies.[47] The cycling stability of the SC was evaluated over 10 000 charge–discharge cycles at 2.5 A g^{-1} between 0 and 2.5 V at room temperature. PEIS was conducted with an oscillating amplitude of 10 mV, collecting impedance spectra in a logarithmic manner across 0.1 MHz to 0.1 Hz, with ten points per decade.

[1] K. Poonam, A. Sharma, S. K. Arora, *J. Energy Storage* **2019**, *21*, 801.
[2] V. Molahalli, K. Chaithrashree, M. K. Singh, M. Agrawal, S. G. Krishnan, G. Hegde, *J. Energy Storage* **2023**, *70*, 108062.
[3] K. Dissanayake, D. Kularatna-Abeywardana, *J. Energy Storage* **2024**, *96*, 112563.
[4] J. Lu, J. Zhang, X. Wang, J. Zhang, Z. Tian, E. Zhu, L. Yang, X. Guan, H. Ren, J. Wu, X. Li, G. Wang, *J. Energy Storage* **2024**, *103*, 114338.
[5] C. Xiong, Y. Zhang, Y. Ni, *J. Power Sources* **2023**, *560*, 232698.
[6] T. Guo, D. Zhou, L. Pang, S. Sun, T. Zhou, J. Su, *Small* **2022**, *18*, 2106360.
[7] T. S. Bhat, P. S. Patil, R. B. Rakhi, *J. Energy Storage* **2022**, *50*, 104222.
[8] J. Chen, S. Lei, S. Zhang, C. Zhu, Q. Liu, C. Wang, Z. Zhang, S. Wang, Y. Shi, L. Yin, R. Wang, *Adv. Funct. Mater.* **2023**, *33*, 2215027.
[9] S. V. Doronin, M. A. Nazarov, *J. Phys. Chem. C* **2022**, *126*, 14611.
[10] M. Armand, F. Endres, D. R. MacFarlane, H. Ohno, B. Scrosati, *Nat. Mater.* **2009**, *8*, 621.
[11] X. Tian, Q. Zhu, B. Xu, *ChemSusChem* **2021**, *14*, 2501.
[12] M. Raghibi, G. Nikiforidis, M. Anouti, *ChemElectroChem* **2023**, *10*, e202300183.
[13] C. Tachouaft, H. Kahri, L. Wang, G. Nikiforidis, M. Anouti, *Batter. Supercaps* **2024**, *7*, e202300560.
[14] S. Liu, R. Klukas, T. Porada, K. Furda, A. M. Fernández, A. Balducci, *J. Power Sources* **2022**, *541*, 231657.
[15] X. Solans, C. Gonzalez-Silgo, C. Ruiz-Pérez, *J. Solid State Chem.* **1997**, *131*, 350.
[16] T. S. Shyju, S. Anandhi, R. Gopalakrishnan, *CrystEngComm* **2012**, *14*, 1387.
[17] E. Lemaire, D. Thuau, M. Souêtre, L. Zgainski, A. Royet, A. Atli, *Sens. Actuators A Phys.* **2021**, *318*, 112483.
[18] M. Wu, *Nat. Rev. Phys.* **2021**, *3*, 726.
[19] S. Verma, S. Arya, V. Gupta, A. Khosla, *Chem. Eng. J.* **2021**, *424*, 130567.
[20] M. Saitou, *Int. J. Electrochem. Sci.* **2018**, *13*, 3326.
[21] V. Mathivanan, M. Haris, J. Chandrasekaran, *Optik* **2016**, *127*, 1804.
[22] O. Taeri, A. Hassanzadeh, F. Ravari, *ChemElectroChem* **2020**, *7*, 2123.
[23] V. Mathivanan, M. Haris, *Spectrochim. Acta A Mol. Biomol. Spectrosc.* **2013**, *102*, 341.
[24] M. Laliberte, W. E. Cooper, *J. Chem. Eng. Data* **2004**, *49*, 1141.
[25] H. Ahn, D. Kim, M. Lee, K. W. Nam, *Commun. Mater.* **2023**, *4*, 37.
[26] G. Nikiforidis, M. El Yagoubi, M. Anouti, *Electrochim. Acta* **2022**, *402*, 139529.
[27] I. Popov, Z. Zhu, A. R. Young-Gonzales, R. L. Sacci, E. Mamontov, C. Gainaru, S. J. Paddison, A. P. Sokolov, *Commun. Chem.* **2023**, *6*, 77.
[28] J. Pires, L. Timperman, J. Jacquemin, A. Balducci, M. Anouti, *J. Chem. Thermodyn.* **2013**, *59*, 10.
[29] S. Amara, W. Zaidi, L. Timperman, G. Nikiforidis, M. Anouti, *J. Chem. Phys.* **2021**, *154*, 164708.
[30] A. Yllö, C. Zhang, *Chem. Phys. Lett.* **2019**, *729*, 6.
[31] M. Sajjad, M. I. Khan, F. Cheng, W. Lu, *J. Energy Storage* **2021**, *40*, 102729.
[32] W. Good, D. B. Ingham, *Electrochim. Acta* **1975**, *20*, 57.
[33] M. Yoshizawa, W. Xu, C. A. Angell, *J. Am. Chem. Soc.* **2003**, *125*, 15411.

[34] A. A. Chialvo, O. D. Crisalle, *J. Phys. Chem. B* **2021**, *125*, 12028.

[35] Q. Zhang, B. Yan, L. Feng, J. Zheng, B. You, J. Chen, X. Zhao, C. Zhang, S. Jiang, S. He, *Nanoscale* **2022**, *14*, 8216.

[36] J. Kleinheins, N. Shardt, M. El Haber, C. Ferronato, B. Nozière, T. Peter, C. Marcolli, *Phys. Chem. Chem. Phys.* **2023**, *25*, 11055.

[37] L. Suo, O. Borodin, T. Gao, M. Olguin, J. Ho, X. Fan, C. Luo, C. Wang, K. Xu, *Science* **2015**, *350*, 938.

[38] G. Nikiforidis, S. Phadke, M. Anouti, *Adv. Mater. Interfaces* **2023**, *10*, 2202046.

[39] S. J. Rajasekaran, A. N. Grace, G. Jacob, A. Alodhayb, S. Pandiaraj, V. Raghavan, *Catalysts* **2023**, *13*, 286.

[40] F. Barzegar, D. Y. Momodu, O. O. Fashedemi, A. Bello, J. K. Dangbegnon, N. Manyala, *RSC Adv.* **2015**, *5*, 107482.

[41] Q. Gao, *J. Energy Chem.* **2019**, *38*, 219.

[42] J. Kang, S. H. Jayaram, J. Rawlins, J. Wen, *Electrochim. Acta* **2014**, *144*, 200.

[43] S.-W. Xu, M.-C. Zhang, G.-Q. Zhang, J.-H. Liu, X.-Z. Liu, X. Zhang, D.-D. Zhao, C.-L. Xu, Y.-Q. Zhao, *J. Power Sources* **2019**, *441*, 227220.

[44] J. Fischer, B. Pohle, E. Dmitrieva, K. Thümmler, S. Fischer, D. Mikhailova, *J. Energy Storage* **2022**, *55*, 105725.

[45] T. Subramaniam, M. N. M. Ansari, S. G. Krishnan, M. Khalid, *Chemosphere* **2024**, *354*, 141593.

[46] J. Chidiac, G. Nikiforidis, L. Timperman, M. Anouti, *ChemPhysChem* **2022**, *23*, e202200224.

[47] G. Nikiforidis, S. Wustoni, D. Ohayon, V. Druet, S. Inal, *ACS Appl. Energy Mater.* **2020**, *3*, 7896.